

Mie Exciton-Polariton in a Perovskite Metasurface

Khalil As’ham¹, Ibrahim Al-Ani¹, Wen Lei², Haroldo T. Hattori¹, Lujun Huang^{1,*} and Andrey Miroshnichenko^{1,†}

¹*School of Engineering and Information Technology, University of New South Wales at Canberra, Northcott Drive, Canberra, Australian Capital Territory 2610, Australia*

²*Department of Electrical Engineering, School of Engineering, University of Western Australia, 35 Stirling Highway, Perth, Washington 6009, Australia*



(Received 2 April 2022; revised 16 May 2022; accepted 25 May 2022; published 29 July 2022)

Exciton-polariton arising from strong light-matter interaction between exciton and optical cavity has attracted considerable attention due to its potential applications in Bose-Einstein condensation, low-threshold lasing, and slow light. In recent years, two-dimensional lead halide perovskite has emerged as an ideal candidate for realizing exciton polariton at room temperature because it has large exciton binding energy and quantum yield. Here, we demonstrate that strong coupling could be enabled with a perovskite metasurface that supports multipolar Mie resonance, including magnetic quadrupole dominant, anapole, and toroidal resonances. For an array of perovskite nanodisks, the strong coupling behavior between these resonances and exciton is confirmed by the anticrossing features in absorption spectra mapping, while the Rabi splitting is increased from 230.7 meV in magnetic quadrupole-exciton strong coupling to 253 meV in both anapole-exciton and toroidal-exciton strong coupling. The enhanced Rabi splitting is attributed to the stronger field localization within the perovskite instead of within the air gap. In addition, we find that the Rabi splitting depends on the oscillatory strength of the exciton mode and can then be boosted to 362 meV in anapole-exciton strong coupling. Our results provide promising ways to improve the performance of optoelectronic devices such as low-threshold lasers and slow-light devices.

DOI: [10.1103/PhysRevApplied.18.014079](https://doi.org/10.1103/PhysRevApplied.18.014079)

I. INTRODUCTION

Exciton polaritons, formed by the interaction between excitons and light, are critical quasiparticles used in different applications such as Bose-Einstein condensation, superfluidity, quantum vortices, low-threshold lasing, sensing, and slow light [1–5]. So far, most studies on exciton polaritons focus on conventional inorganic semiconductors such as gallium arsenide (GaAs) and cadmium telluride (CdTe) [6]. However, observing exciton polaritons in inorganic materials at room temperature is challenging because of their small excitonic energy, weak oscillator strength, and large size [7,8]. Although efforts to implement such devices that operate at room temperature have been made with inorganic and organic materials with high excitonic binding energy such as gallium nitride (GaN), zinc oxide (ZnO), and organic semiconductors, they still suffer from mismatched thermal expansion coefficients, require high-temperature epitaxial techniques, and have large sizes [6–9]. Recently, pushing the interaction between the exciton and electromagnetic waves down to the nanoscale at room temperature has drawn

much attention due to its various applications that lead to the implementation of unconventional nanophotonic devices [10].

In principle, surface plasmon polariton nanostructures have the ability to confine light in tiny volumes, potentially being an ideal platform to explore the strong-coupling regime [11]. Of note, the interaction between plasmon modes and exciton in molecules, quantum dots, and transition metal dichalcogenides (TMDCs) have been observed at room temperature at the nanoscale [12–18]. However, both molecules and quantum dots can hardly control the excitonic orientation [17]. Moreover, the metallic plasmonic structures suffer from high absorption and large Ohmic losses [10,19], which may degrade the device’s performance operating at considerable pumping power.

In recent years, hybrid organic-inorganic lead halide perovskites materials have emerged as an excellent platform to realize photonic and optoelectronic devices with superior performance due to their salient properties, such as high optical absorption efficiency, broad resonance tunability, large excitonic binding energy, cheap fabrication techniques, and low rates of nonradiative recombination compared with conventional semiconductor materials [2,3,20–25]. These features make it possible to observe the strong-coupling regime at room temperature and have led

*ljhuang@mail.sitp.ac.cn

†andrey.miroshnichenko@adfa.edu.au

to the realization of laser, photodetectors, and solar cells [7,26–36]. The strong-coupling regime between the exciton and electromagnetic waves has been observed using two-dimensional (2D) perovskite materials in different cavities. For example, a Fabry-Perot microcavity, which consists of 2D perovskite material embedded between two distributed Bragg reflectors (DBRs), is utilized to observe exciton polaritons with large Q factor (larger than 2000) [37]. Moreover, exciton polaritons are also observed in plasmonic nanocavities and whispering-gallery-mode cavity [3,28,34,37–44]. However, all these observations in exciton still suffer from either the heat generation in the noble metals or complex fabrication process of growing the DBR mirrors.

Consequently, a good alternative to implementing a photonic cavity is an all-dielectric metasurface made of high-refractive-index materials. All-dielectric metasurface has demonstrated its powerful capability of enhancing light-matter interaction because it supports both electric and magnetic Mie resonances [45,46]. Due to these remarkable advantages of using optical resonances in all-dielectric metasurface, observing exciton polaritons in all perovskite cavities can address the challenges faced by the aforementioned cavities. Although several studies have implemented all-perovskite metasurface in realizing strong coupling [1,34], achieving and maximizing the strong coupling between Mie resonance and perovskite exciton remains an open question with all-perovskite metasurface.

This work demonstrates strong light-matter interaction between the exciton and multipolar Mie resonance by taking advantage of perovskite's high refractive index. The behavior of strong coupling between exciton and magnetic quadrupole resonance supported by an array of perovskite nanodisks, is evidenced by an anticrossing in the absorption spectrum, accompanied by a retrieved Rabi splitting 230.7 meV. Moreover, we found Rabi splitting can be further improved to 253 meV by increasing the index contrast between patterned perovskite and substrate with a refractive index close to unity or by adding a perovskite film underneath the nanodisk arrays. In these cases, strong coupling happens between either exciton and anapole or exciton and toroidal dipole resonance. The larger Rabi splitting is attributed to the considerable field enhancement within the perovskite instead of the air gap between nanodisks. We also find that Rabi splitting can be modulated by the oscillator strength of 2D perovskite materials for the exciton. Our results may pave the way for developing high-performance photonic devices based on all-perovskite metasurface.

II. RESULTS AND DISCUSSION

A perovskite material phenethylammonium lead iodide (PEPI) with the chemical formula $(C_6H_5C_2H_4NH_3)_2PbI_4$

is chosen as an active medium because it has a large exciton binding energy. The devices are designed and simulated by using different software packages, including FDTD Lumerical, COMSOL and RCWA in MATLAB. In our simulations, the PEPI data was extracted from the paper by Lu *et al.* [1] (see Sec. S1 within the Supplemental Material [47]).

A series of PEPI nanodisks arranged in a square lattice on a glass substrate are shown in Fig. 1(a). The cylindrical geometry is chosen due to the ease of fabricating and flexibility of tuning Mie resonances by varying its geometry parameters such as period (P), height (H), and radius (R) [10]. The period and nanodisks' radius are fixed at 320 and 142 nm, respectively, whereas the nanodisk height is varied from 200 to 300 nm as shown in the lossless reflection spectra in Fig. 1(b) (we artificially remove PEPI losses in these simulations to tune the resonance wavelength of the disks better). As the height increases, Mie resonance shows redshifts. Also, it can be seen that the Q factor of the resonance is increased as the nanodisk height increases, which makes this resonance suitable for designing devices requiring high Q factors such as semiconductor lasers (see Sec. S2 and Sec. 3 within the Supplemental Material [47–49]). To unveil the physical nature of this Mie resonance, multipole decompositions are studied at 255-nm nanodisk thickness. The scattered power plotted in Fig. 1(c) shows that magnetic quadrupole (MQ) is the dominant multipole among other moments. The exciton of PEPI material is found at 2.4 eV so that the MQ dominant resonance can be shifted to lower wavelengths by varying PEPI nanodisk radius between 120 and 150 nm as observed in the reflection spectra shown in Fig. 1(d). In contrast, the height and period are fixed at 255 and 320 nm, respectively. For a nanodisk with a radius of 132 nm, the MQ-dominant resonance is aligned to the exciton resonance 2.4 eV of perovskite, as presented in plotted reflection spectra in Fig. 1(e). This resonance exhibits electric and magnetic fields' enhancement by 51.6 and 16.7 folds, respectively, as shown in Fig. 1(f).

To investigate the strong coupling between Mie resonance and exciton supported by the PEPI nanodisk, the loss of both index material and exciton resonance are now included in absorption calculations. The existence of an exciton resonance and MQ-dominant resonance in the same PEPI nanodisks' lattice suggest that they can be strongly coupled with each other by changing the nanodisk radius so that the MQ-dominant resonance is tuned to overlap with the exciton mode, leading to the emergence of anticrossing behavior in the absorption spectrum mapping shown in Fig. 2(a). At the anticrossing point between Mie resonance and exciton modes (132-nm nanodisk radius) shown in Fig. 2(b), the absorption spectrum describes three peaks that correspond to upper branch, lower branch, and exciton as depicted in Fig. 2(c).

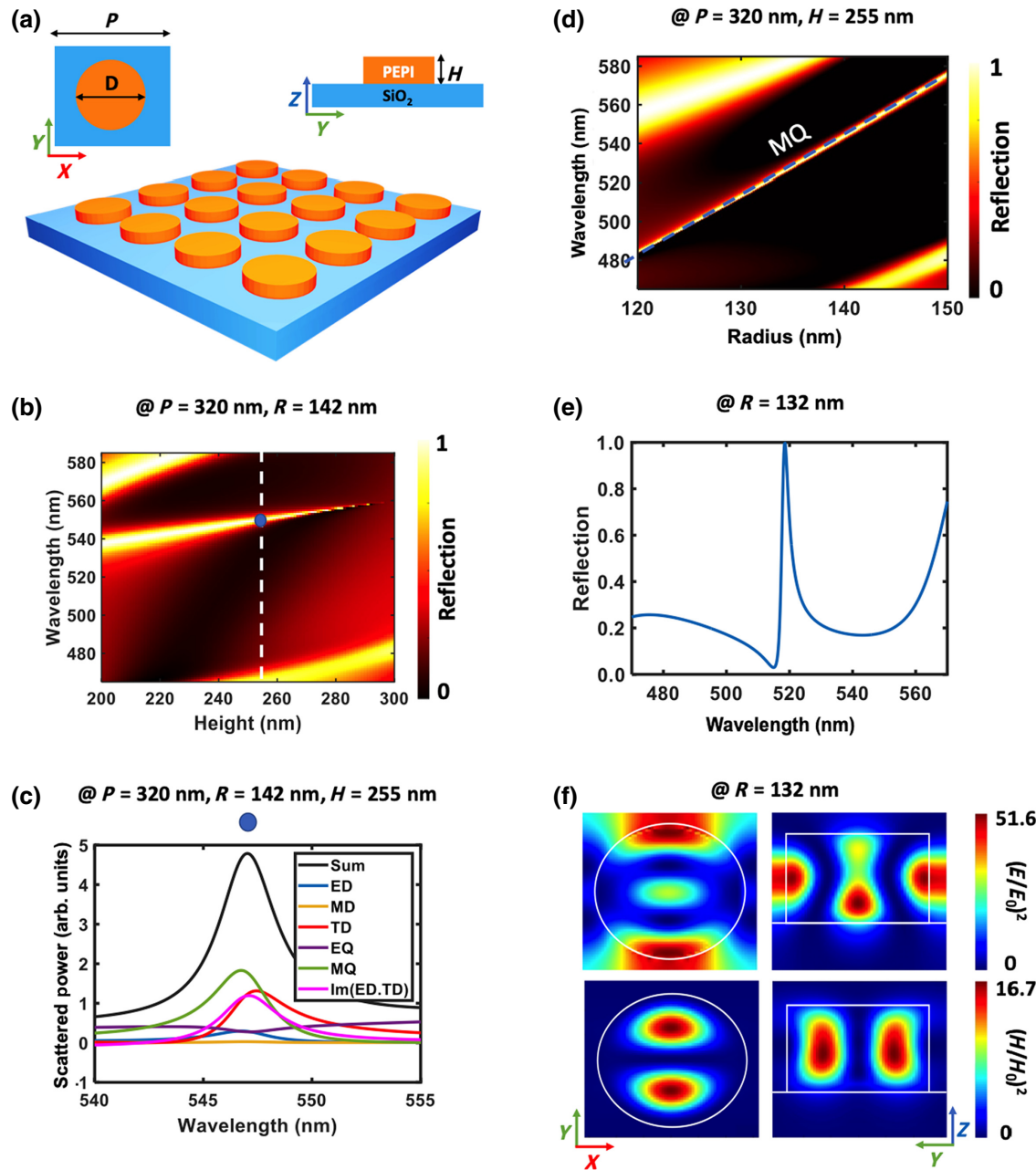


FIG. 1. (a) Schematic of an array PEPI nanodisk on a glass substrate with the specific period (P), diameter (D), and height (H). (b) A reflection spectra at $P = 320$ nm, radius (R) = 142 nm, and H ranging from 200 to 300 nm. (c) Calculated multipole decompositions presented in scattered power plot. (d) Calculated lossless reflection spectrum with different PEPI nanodisk radii from 120 to 150 nm at constant $P = 320$ nm and $H = 255$ nm. (e) Reflection spectrum at 517 nm for MQ-dominant resonance. (f) Electric field and magnetic field distributions at MQ-dominant resonance.

A two-coupled-oscillator model of Hamiltonian is used to verify that the MQ-exciton interaction reaches the strong coupling regime. The model can be described as [50]

$$\begin{pmatrix} E_M - i\hbar\Gamma_M & g_{MX} \\ g_{MX} & E_X - i\hbar\Gamma_X \end{pmatrix} \begin{pmatrix} \alpha \\ \beta \end{pmatrix} = E \begin{pmatrix} \alpha \\ \beta \end{pmatrix}, \quad (1)$$

where E_M and E_X are energies of the Mie resonance and exciton modes in the uncoupled initial states; g_{MX} is the coupling strength between the Mie resonance and the exciton; $\hbar\Gamma_M$ and $\hbar\Gamma_X$ are the half-widths at half-maximum (HWHM) of MQ resonance and exciton mode; α and β are the eigenvectors of the upper and lower polariton branches. The eigenvalues E_{\pm} of the upper and lower polaritons are calculated when the eigenvector satisfies the condition

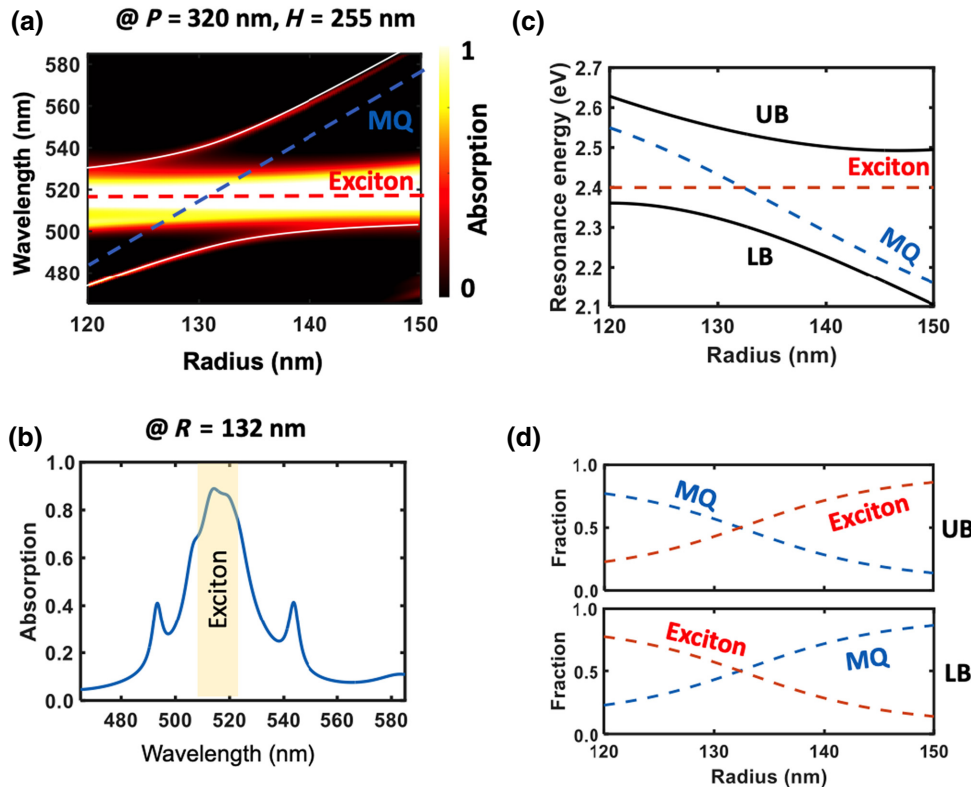


FIG. 2. (a) Absorption color map with different nanodisk radii ranging from 120 to 150 nm for MQ-exciton strong coupling. (b) MQ-exciton strong coupling at the anticrossing point with lower peak, exciton, and upper peak. (c) Dispersion curve of MQ-exciton strong coupling, where the blue and red dashed lines exhibit the uncoupled MQ-dominant resonance and exciton, respectively. (d) Hopfield coefficients for MQ-exciton strong coupling.

$|\alpha|^2 + |\beta|^2 = 1$ as described in the following equation:

$$E_{\pm} = \frac{1}{2} [(E_M + E_X - i\hbar\Gamma_X - i\hbar\Gamma_M) \pm \sqrt{4g_{MX}^2 + [E_M - E_X - i(\hbar\Gamma_X - \hbar\Gamma_M)]^2}]. \quad (2)$$

When the energies of Mie resonance and exciton mode are equal, the Rabi splitting is defined by

$$\hbar\Omega_{MX} = \sqrt{4g_{MX}^2 - (\hbar\Gamma_X - \hbar\Gamma_M)^2}. \quad (3)$$

The calculated Rabi splitting must satisfy two essential conditions to verify that the system is in a strong-coupling regime as described in the following equation:

$$\begin{aligned} g_{MX} &> \frac{1}{2} |\hbar\Gamma_X - \hbar\Gamma_M| \text{ and } g_{MX} \\ &> \sqrt{\frac{1}{2}(\hbar\Gamma_X)^2 + \frac{1}{2}(\hbar\Gamma_M)^2}. \end{aligned} \quad (4)$$

The first condition ensures that the Rabi splitting is non-vanishing, and the second condition ensures that the Rabi splitting can be experimentally observed.

In our case, the eigenvalues E_{\pm} (UB and LB) for MQ resonance are fitted as shown in Fig. 2(c). The difference between the upper polariton branch (UB) and lower polariton branch (LB) at the anticrossing point in the fitted data are the Rabi splitting of MQ-exciton strong coupling ($\hbar\Omega_{MX} = 230.7$ meV) when $\hbar\Gamma_X = 15$ meV and $\hbar\Gamma_M = 8.346$ meV. The coupling strength $g_{MX} = 115.4$ meV is calculated by Eq. (3). The eigenvectors in Fig. 2(d) indicate that there is intermixing behavior between the Mie resonance and exciton mode. Using Eq. (4), MQ-exciton interaction results in a strong-coupling regime with Rabi splitting equal to 230.7 meV.

Figure 1(f) shows that a large portion of the electric field is localized in the air gap between nanodisks and does not contribute to the strong coupling. To further improve the Rabi splitting between Mie resonance and exciton, one way to replace the glass substrate with an aerogel silica substrate with an ultrathin refractive index (1.08). Due to the increased index contrast between perovskite and the substrate, the electric field is mainly confined inside the nanodisk instead of leaking into the air gap. This directly results in enhanced Rabi splitting. Figure 3(a) shows an array of PEPI nanodisks on aerogel substrate with a period of 366 nm, nanodisk height of 136 nm, and nanodisk

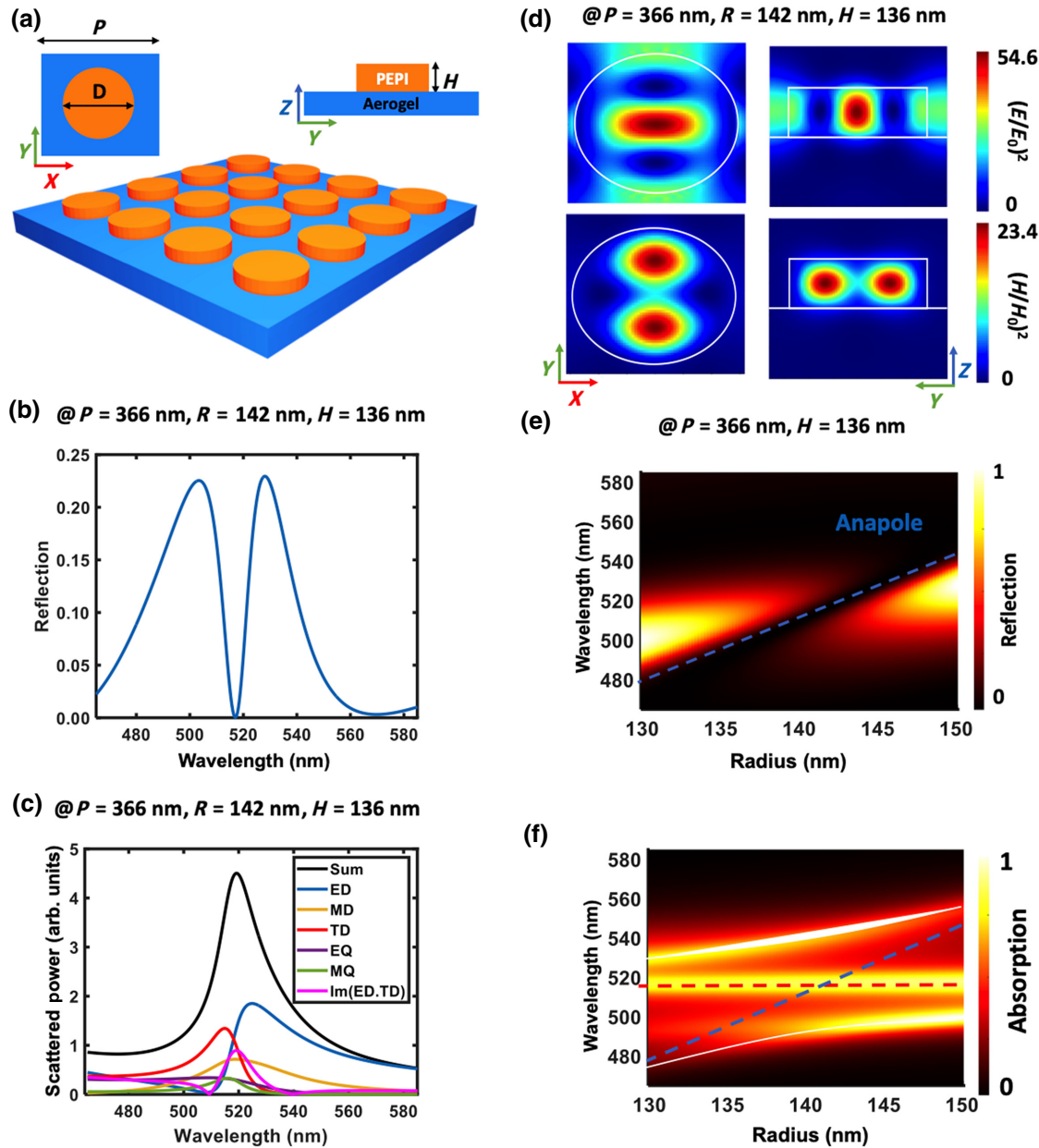


FIG. 3. (a) Schematic of an array PEPI nanodisk on an Aerogel silica substrate. (b) A reflection spectra at $P = 366 \text{ nm}$, $R = 142 \text{ nm}$, and $H = 136 \text{ nm}$. (c) Calculated multipole decompositions presented in scattered power plot. (d) Electric field and magnetic field distributions at anapole mode. (e) Lossless reflection spectrum with different PEPI nanodisk radii from 130 to 150 nm at constant $P = 366 \text{ nm}$ and $H = 136 \text{ nm}$. (f) Loss-absorption color map with different nanodisk radii ranging from 130 to 150 nm for anapole-exciton strong coupling.

radius of 142 nm. A dip in the reflection spectrum presented in Fig. 3(b) refers to anapole mode produced by destructive interference between electric dipole (ED) and toroidal dipole (TD) [51–54] as shown in Fig. 3(c). The anapole mode can confine energy inside the nanodisk and enhance both electric and magnetic fields to 54.6 and 23.4, as shown in Fig. 3(d), respectively. Also, anapole mode can be tuned by varying nanodisk radius from 130 to 150 nm, as depicted in Fig. 3(e). By including the loss in perovskite

material, an anticrossing behavior is indicated in Fig. 3(f) due to the strong coupling between anapole mode and exciton. This strong coupling is analyzed using a two coupled oscillator model as shown in Fig. S4 (see Sec. S4 within the Supplemental Material [47]). The analysis proved that the system falls within a strong-coupling regime with Rabi splitting of 253 meV.

Another way to boost the strong-coupling strength given by the Rabi splitting between Mie resonance and exciton

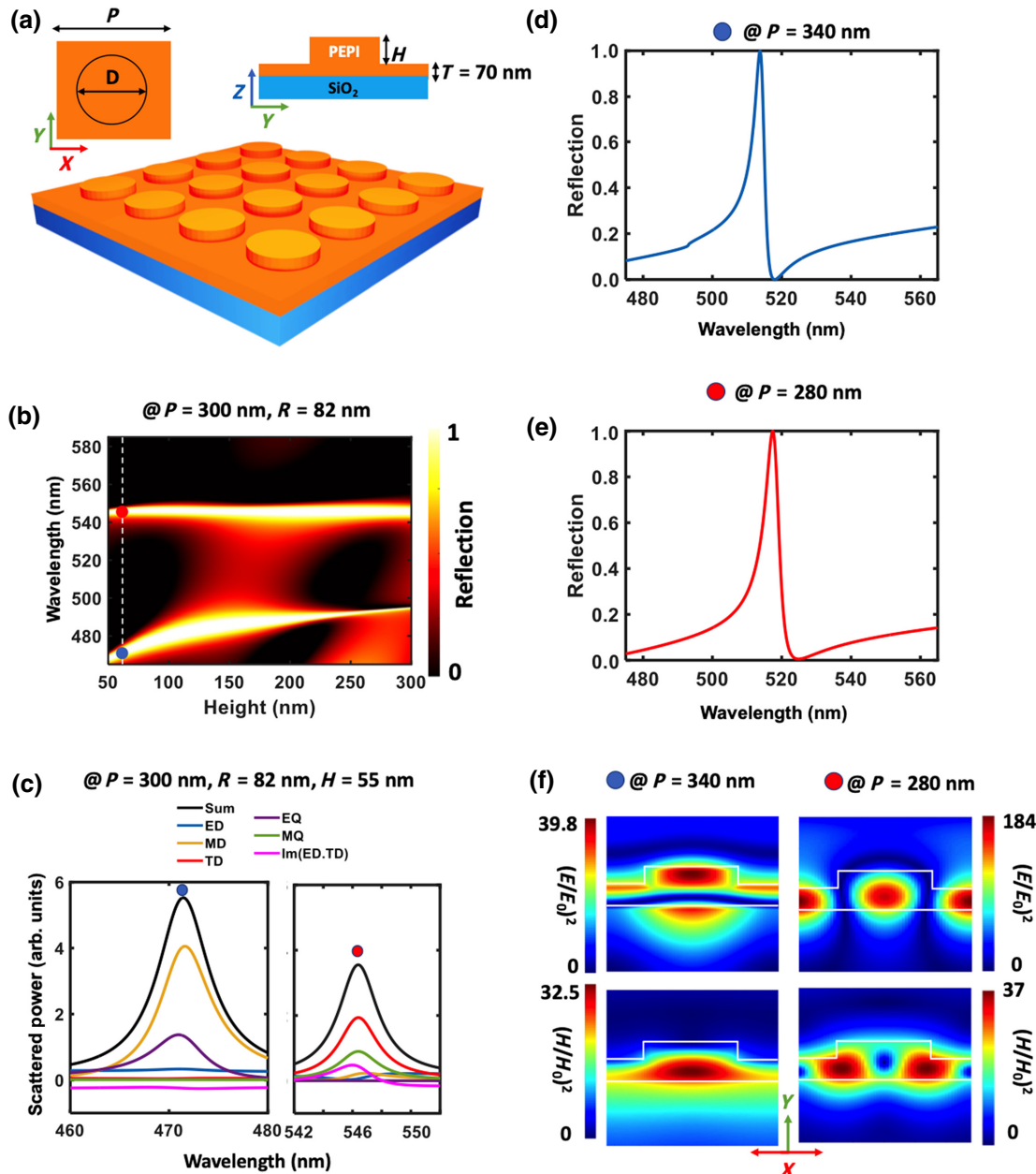


FIG. 4. (a) Schematic of an array PEPI nanodisks with a PEPI film on a glass substrate with the specific period (P), radius (R), height (H), and film thickness (T). (b) A reflection spectra at $P = 300 \text{ nm}$, $R = 82 \text{ nm}$, and H ranging from 50 to 300 nm. (c) Multipole decomposition at $P = 300 \text{ nm}$, $R = 82 \text{ nm}$, and $H = 55 \text{ nm}$. (d), (e) are reflection spectrum at 517 nm for MD and TD, respectively. (f) Electric field and magnetic field distribution at 517 nm wavelength for MD and TD, respectively.

in bulk PEPI nanostructure, is by embedding a PEPI film below the nanodisks' array as presented in the schematic shown in Fig. 4(a). The film thickness (T), lattice period (P), and nanodisk radius (R) are fixed at 70 nm, 300 nm, and 82 nm, respectively. The nanodisk height is varied from 50 to 300 nm to tune the Mie resonances as depicted in the reflection spectrum in Fig. 4(b). Two Mie resonances tuned in the reflection spectrum are referred to as MD and TD as plotted in the multipole decomposition in Fig. 4(c).

By shifting both resonances to the exciton resonance at 517 nm, the electric and magnetic field distributions in Fig. 4(f) confirm that the resonances are referred to as MD and TD. Figures 4(d) and 4(e) present the reflection spectra of both resonances. The electric field and magnetic field of TD resonance are enhanced to 184 and 37, respectively, compared with the previous structure.

Interestingly, electric field enhancement shows a strong dependence on the film thickness as shown in Fig. S5(c)

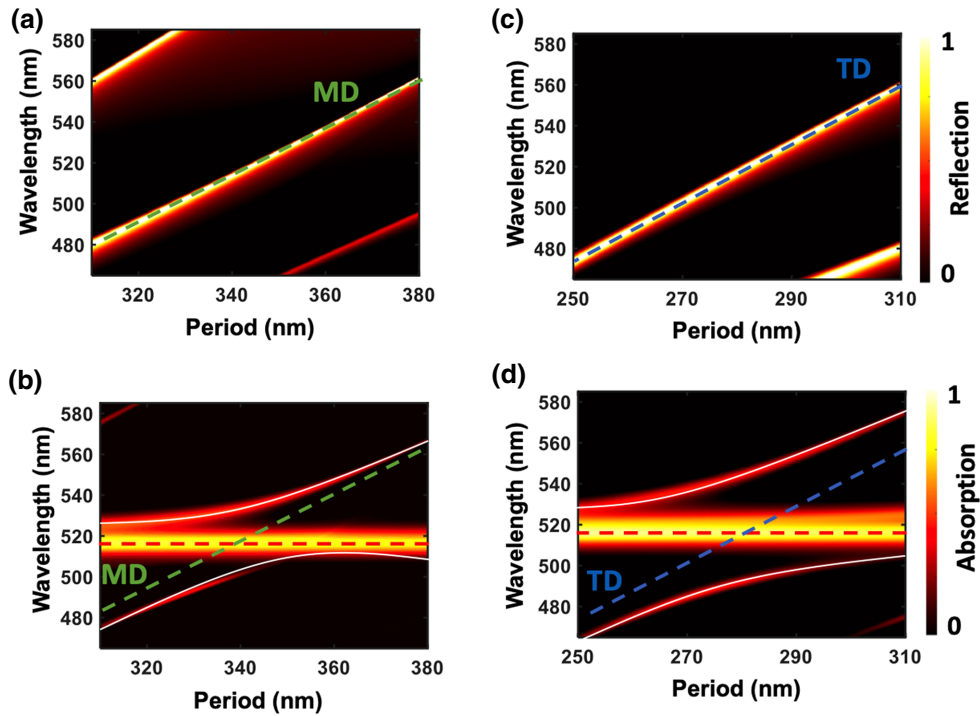


FIG. 5. (a), (c) Reflection spectrum maps for MD and TD resonances when the lattice period varied from 250 to 380 nm. (b), (d) Absorption spectrum maps for MD and TD resonances coupled with exciton mode.

within the Supplemental Material [47]. However, as the thickness increased, the TD resonance became close to the MD resonance. Consequently, a thickness of 70 nm is chosen to ensure that TD is far enough from MD resonance and to observe a strong coupling regime with only one resonance, as shown in Figs. S5(a) and S5(b) (see Sec. S5 within the Supplemental Material [47]).

Note that both MD and TD resonances could be used to achieve strong coupling by varying the lattice period. It is clearly seen from Figs. 5(a)–5(c) that these two resonances can cross the exciton wavelength of 517 nm. After including the loss in perovskite, we can find that the strong coupling indeed happens in both cases due to the anti-crossing features in the absorption spectra mapping shown in Figs. 5(b)–5(d). Again, we use the aforementioned two coupled oscillator model to extract the Rabi splitting and exciton-polariton eigenstates. The analyses in Fig. S6 within the Supplemental Material shows that Rabi-splitting values of the MD-exciton and TD-exciton interactions are 148.4 and 253 meV, respectively (see Sec. S6 within the Supplemental Material [47]). Given that the HWHM of MD and TD are 11 and 13.3 meV, calculated Rabi splitting for both MD-exciton and TD-exciton interactions indicates these two systems fall within a strong-coupling regime.

Although absorption spectra are used to observe MQ-exciton, anapole-exciton, MD-exciton, and TD-exciton strong coupling, the PL spectra serve as strong evidence of strong coupling between Mie resonance and exciton.

Since the PL emission is proportional to the Purcell factor, we calculate the Purcell factor (P_F , indicating emission rate enhancement) and fluorescence enhancement (F_E) to prove the anticrossing behavior in PL spectra. Purcell factor and fluorescence enhancement can be expressed as follows [55]:

$$P_F = \frac{P_{\text{dipole}}}{P_{\text{radiated}}^0}, \quad (5)$$

$$F_E = P_F \times \frac{Q_E}{Q_{E_0}}, \quad (6)$$

where P_{dipole} , P_{radiated}^0 , Q_E , and Q_{E_0} are dipole-radiated power in an inhomogeneous environment, dipole-radiated power in a homogeneous environment, quantum efficiency, and intrinsic quantum efficiency, respectively. Figure S7 within the Supplemental Material presents an obvious anti-crossing behavior for MQ exciton, anapole exciton, MD exciton, and TD exciton in both Purcell factor and fluorescence enhancement mapping (see Sec. S7 within the Supplemental Material [47]). Therefore, all systems indeed fall within the strong-coupling regime. Additionally, both reflection and transmission spectra mapping show anti-crossing behavior as presented in Fig. S8 within the Supplemental Material (see Sec. S8 within the Supplemental Material [47,56]).

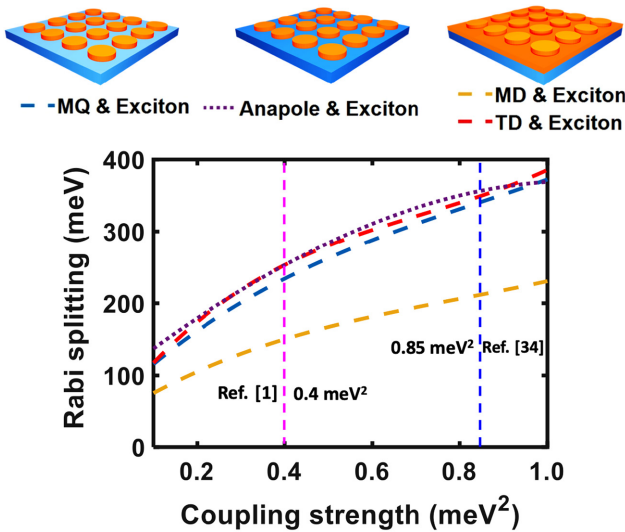


FIG. 6. Enhancement of the Rabi splitting with varying oscillator strength from 0.1 to 1 meV² for three structures. Dark blue dashes present the MQ-exciton strong coupling, purple dots present anapole-exciton strong coupling, orange dashes exhibit MD-exciton strong coupling, the red dashed line depicts TD-exciton strong coupling, the magenta dashed line presents the coupling strength used by Ref. [1], and the light-blue dashed line presents the coupling strength used by Ref. [34].

To compare our results with the results reported in previous studies, the oscillator strength is artificially tuned from 0.1 to 1 meV² as presented in Fig. 6. It can be seen that the Rabi splitting increases as the oscillator strength increases for all exciton polaritons used in this paper. At oscillator strength 0.4 meV², the largest Rabi splitting with 253 meV is observed in anapole-exciton and TD-exciton strong coupling that is larger than the Rabi splitting reported in Ref. [1]. At oscillator strength 0.85 meV², the Rabi splitting of anapole-exciton strong coupling is boosted to 362 meV. In contrast, TD-exciton strong coupling is increased to 360 meV, which are also larger than the reported Rabi splitting in Ref. [34].

III. CONCLUSIONS

In conclusion, strong coupling between multipolar Mie resonance and exciton has been demonstrated within an array of PEPI nanodisks with a Rabi splitting of 230.7 meV. It can be mainly attributed to the large field enhancement of Mie resonance. Replacing the glass substrate with aerogel silica substrate allows the perovskite material to confine extra energy inside the nanodisk array and then boost the Rabi splitting to 253 meV. Moreover, embedding a PEPI film underneath the rectangular lattice introduces a strong light-matter interaction between toroidal-dipole resonance and exciton, accompanied by Rabi splitting of 253 meV. The improved field confinement can explain the enhancement of Rabi splitting within

the perovskite materials in an all-perovskite metasurface. Besides, it is found that the Rabi splitting is further increased to 362 meV at oscillator strength 0.85 meV² when compared with previous studies.

ACKNOWLEDGMENTS

This work is supported by the Australian Research Council (DP200101353).

- [1] L. Lu, Q. Le-Van, L. Ferrier, E. Drouard, C. Seassal, and H. S. Nguyen, Engineering a light-matter strong coupling regime in perovskite-based plasmonic metasurface: Quasi-bound state in the continuum and exceptional points, *Photonics Res.* **8**, A91 (2020).
- [2] W. Du, S. Zhang, Q. Zhang, and X. Liu, Recent progress of strong exciton–photon coupling in lead halide perovskites, *Adv. Mater.* **31**, 1804894 (2019).
- [3] A. Fieramosca, L. Polimeno, V. Ardizzone, L. De Marco, M. Pugliese, V. Maiorano, M. De Giorgi, L. Dominici, G. Gigli, D. Gerace, D. Ballarini, and D. Sanvitto, Two-dimensional hybrid perovskites sustaining strong polariton interactions at room temperature, *Sci. Adv.* **5**, eaav9967 (2019).
- [4] M. Qin, S. Xiao, W. Liu, M. Ouyang, T. Yu, T. Wang, and Q. Liao, Strong coupling between excitons and magnetic dipole quasi-bound states in the continuum in WS₂-TiO₂ hybrid metasurfaces, *Opt. Express* **29**, 18026 (2021).
- [5] L. Huang, A. Krasnok, A. Alu, Y. Yu, D. Neshev, and A. Miroshnichenko, enhanced light-matter interaction in two-dimensional transition metal dichalcogenides, *Rep. Prog. Phys.* **85**, 046401 (2021).
- [6] R. Su, C. Diederichs, J. Wang, T. C. H. Liew, J. Zhao, S. Liu, W. Xu, Z. Chen, and Q. Xiong, Room-temperature polariton lasing in all-inorganic perovskite nanoplatelets, *Nano Lett.* **17**, 3982 (2017).
- [7] R. Su, S. Ghosh, J. Wang, S. Liu, C. Diederichs, T. C. H. Liew, and Q. Xiong, Observation of exciton polariton condensation in a perovskite lattice at room temperature, *Nat. Phys.* **16**, 301 (2020).
- [8] Q. Shang, S. Zhang, Z. Liu, J. Chen, P. Yang, C. Li, W. Li, Y. Zhang, Q. Xiong, X. Liu, and Q. Zhang, Surface plasmon enhanced strong exciton–photon coupling in hybrid inorganic–organic perovskite nanowires, *Nano Lett.* **18**, 3335 (2018).
- [9] S. Zhang, Q. Shang, W. Du, J. Shi, Z. Wu, Y. Mi, J. Chen, F. Liu, Y. Li, M. Liu, Q. Zhang, and X. Liu, Strong exciton–photon coupling in hybrid inorganic–organic perovskite micro/nanowires, *Adv. Opt. Mater.* **6**, 1701032 (2018).
- [10] F. Todisco, R. Malureanu, C. Wolff, P. A. D. Gonçalves, A. S. Roberts, N. A. Mortensen, and C. Tserkezis, Magnetic and electric Mie-exciton polaritons in silicon nanodisks, *Nanophotonics* **9**, 803 (2020).
- [11] S.-D. Liu, J.-L. Fan, W.-J. Wang, J.-D. Chen, and Z.-H. Chen, Resonance coupling between molecular excitons and nonradiating anapole modes in silicon nanodisk-J-aggregate heterostructures, *ACS Photonics* **5**, 1628 (2018).

- [12] H. Zhang, B. Abhiraman, Q. Zhang, J. Miao, K. Jo, S. Roccasecca, M. W. Knight, A. R. Davoyan, and D. Jariwala, Hybrid exciton-plasmon-polaritons in van der Waals semiconductor gratings, *Nat. Commun.* **11**, 3552 (2020).
- [13] J. Sun, Y. Li, H. Hu, W. Chen, D. Zheng, S. Zhang, and H. Xu, Strong plasmon-exciton coupling in transition metal dichalcogenides and plasmonic nanostructures, *Nanoscale* **13**, 4408 (2021).
- [14] M. Ramezani, A. Halpin, A. I. Fernández-Domínguez, J. Feist, S. R.-K. Rodriguez, F. J. García-Vidal, and J. Gómez Rivas, Plasmon-exciton-polariton lasing, *Optica* **4**, 31 (2017).
- [15] M. de Giorgi, M. Ramezani, F. Todisco, A. Halpin, D. Caputo, A. Fieramosca, J. Gomez-Rivas, and D. Sanvitto, Interaction and coherence of a plasmon-exciton polariton condensate, *ACS Photonics* **5**, 3666 (2018).
- [16] K. As'ham, I. Al-Ani, L. Huang, A. E. Miroshnichenko, and H. T. Hattori, Boosting strong coupling in a hybrid WSe₂ monolayer-anapole-plasmon system, *ACS Photonics* **8**, 489 (2021).
- [17] F. Deng, H. Liu, L. Xu, S. Lan, and A. E. Miroshnichenko, Strong exciton-plasmon coupling in a WS₂ monolayer on Au film hybrid structures mediated by liquid Ga nanoparticles, *Laser Photonics Rev.* **14**, 1900420 (2020).
- [18] I. Al-Ani, K. As'Ham, L. Huang, A. Miroshnichenko, and H. Hattori, Enhanced strong coupling of TMDC monolayers by bound state in the continuum, *Laser Photonics Rev.* **15**, 2100240 (2021).
- [19] G. W. Castellanos, S. Murai, T. V. Raziman, S. Wang, M. Ramezani, A. G. Curto, and J. Gómez Rivas, Exciton-polaritons with magnetic and electric character in all-dielectric metasurfaces, *ACS Photonics* **7**, 1226 (2020).
- [20] Y. Zhou, J. Li, C. Fang, J. Ma, L. Li, and D. Li, Exciton-phonon interaction-induced large in-plane optical anisotropy in two-dimensional all-inorganic perovskite crystals, *J. Phys. Chem. Lett.* **12**, 3387 (2021).
- [21] E. Y. Tiguntseva, D. G. Baranov, A. P. Pushkarev, B. Munkhbat, F. Komissarenko, M. Franckevičius, A. A. Zakhidov, T. Shegai, Y. S. Kivshar, and S. V. Makarov, Tunable hybrid Fano resonances in halide perovskite nanoparticles, *Nano Lett.* **18**, 5522 (2018).
- [22] Q. Zhang, C. Diederichs, and Q. Xiong, Golden hour for perovskite photonics, *Photonics Res.* **8**, PP1 (2020).
- [23] C. Zhang, S. Xiao, Y. Wang, Y. Gao, Y. Fan, C. Huang, N. Zhang, W. Yang, and Q. Song, Lead halide perovskite-based dynamic metasurfaces, *Laser Photonics Rev.* **13**, 1900079 (2019).
- [24] S. Makarov, A. Furasova, E. Tiguntseva, A. Hemmetter, A. Berestennikov, A. Pushkarev, A. Zakhidov, and Y. Kivshar, Halide-perovskite resonant nanophotonics, *Adv. Opt. Mater.* **7**, 1800784 (2019).
- [25] R. Su, A. Fieramosca, Q. Zhang, H. S. Nguyen, E. Deleporte, Z. Chen, D. Sanvitto, T. C. H. Liew, and Q. Xiong, Perovskite semiconductors for room-temperature exciton-polaritonics, *Nat. Mater.* **20**, 1315 (2021).
- [26] A. P. Schlaus, M. S. Spencer, and X.-Y. Zhu, Light-matter interaction and lasing in lead halide perovskites, *Acc. Chem. Res.* **52**, 2950 (2019).
- [27] Q. Zhang, Q. Shang, R. Su, T. T. H. Do, and Q. Xiong, Halide perovskite semiconductor lasers: materials, cavity design, and low threshold, *Nano Lett.* **21**, 1903 (2021).
- [28] Q. Han, J. Wang, J. Lu, L. Sun, F. Lyu, H. Wang, Z. Chen, and Z. Wang, Transition between exciton-polariton and coherent photonic lasing in all-inorganic perovskite microcuboid, *ACS Photonics* **7**, 454 (2020).
- [29] F. Fang, H. Li, S. Fang, B. Zhou, F. Huang, C. Ma, Y. Wan, S. Jiang, Y. Wang, B. Tian, and Y. Shi, 2D Cs₂AgBiBr₆ with boosted light-matter interaction for high-performance photodetectors, *Adv. Opt. Mater.* **9**, 2001930 (2021).
- [30] K. Wang, G. Xing, Q. Song, and S. Xiao, Micro- and nanostructured lead halide perovskites: From materials to integrations and devices, *Adv. Mater.* **33**, 2000306 (2021).
- [31] C. Huang, C. Zhang, S. Xiao, Y. Wang, Y. Fan, Y. Liu, N. Zhang, G. Qu, H. Ji, J. Han, L. Ge, Y. Kivshar, and Q. Song, Ultrafast control of vortex microlasers, *Science* **367**, 1018 (2020).
- [32] A. Zhizhchenko, S. Syubaev, A. Berestennikov, A. Yulin, A. Porfirev, A. Pushkarev, I. Shishkin, K. Golokhvast, A. Bogdanov, A. Zakhidov, A. Kuchmizhak, Y. Kivshar, and S. Makarov, Single-mode lasing from imprinted halide-perovskite microdisks, *ACS Nano* **13**, 4140 (2019).
- [33] A. S. Berestennikov, P. M. Voroshilov, S. V. Makarov, and Y. S. Kivshar, Active meta-optics and nanophotonics with halide perovskites, *Appl. Phys. Rev.* **6**, 031307 (2019).
- [34] N. H. M. Dang, D. Gerace, E. Drouard, G. Trippé-Allard, F. Lédée, R. Mazurczyk, E. Deleporte, C. Seassal, and H. S. Nguyen, Tailoring dispersion of room-temperature exciton-polaritons with perovskite-based subwavelength metasurfaces, *Nano Lett.* **20**, 2113 (2020).
- [35] S. Kim, B. H. Woo, S.-C. An, Y. Lim, I. C. Seo, D.-S. Kim, S. Yoo, Q.-H. Park, and Y. C. Jun, Topological Control of 2D perovskite emission in the strong coupling regime, *Nano Lett.* **21**, 10076 (2021).
- [36] N. H. M. Dang, S. Zanotti, E. Drouard, C. Chevalier, G. Trippé-Allard, M. Amara, E. Deleporte, V. Ardizzone, D. Sanvitto, L. Andreani, C. Seassal, D. Gerace, and H. Nguyen, Realization of polaritonic topological charge at room temperature using polariton bound states in the continuum from perovskite metasurface, *Adv. Opt. Mater.* **10**, 2102386 (2022).
- [37] J. Wang, R. Su, J. Xing, D. Bao, C. Diederichs, S. Liu, T. C. H. Liew, Z. Chen, and Q. Xiong, Room temperature coherently coupled exciton-polaritons in two-dimensional organic-inorganic perovskite, *ACS Nano* **12**, 8382 (2018).
- [38] P. Bouteyre, H. Nguyen, J. Lauret, G. Trippé-Allard, G. Delport, F. Lédée, H. Diab, A. Belarouci, C. Seassal, D. Garrot, F. Bretenaker, and E. Deleporte, Room-temperature cavity polaritons with 3D hybrid perovskite: Toward large-surface polaritonic devices, *ACS Photonics* **6**, 1804 (2019).
- [39] Q. Shang, M. Li, L. Zhao, D. Chen, S. Zhang, S. Chen, P. Gao, C. Shen, J. Xing, G. Xing, B. Shen, X. Liu, and Q. Zhang, Role of the exciton-polariton in a continuous-wave optically pumped CsPbBr₃ perovskite laser, *Nano Lett.* **20**, 6636 (2020).
- [40] W. Du, S. Zhang, J. Shi, J. Chen, Z. Wu, Y. Mi, Z. Liu, Y. Li, X. Sui, R. Wang, X. Qiu, T. Wu, Y. Xiao, Q. Zhang, and X. Liu, Strong exciton-photon coupling and lasing behavior in all-inorganic CsPbBr₃ micro/nanowire Fabry-Pérot cavity, *ACS Photonics* **5**, 2051 (2018).
- [41] A. Fieramosca, L. De Marco, M. Passoni, L. Polimeno, A. Rizzo, B. Rosa, G. Cruciani, L. Dominici, M. De Giorgi,

- G. Gigli, L. Andreani, D. Gerace, D. Ballarini, and D. Sanvitto, Tunable out-of-plane excitons in 2D single-crystal perovskites, *ACS Photonics* **5**, 4179 (2018).
- [42] I. A. M. Al-Ani, K. As'ham, L. Huang, A. E. Miroshnichenko, W. Lei, and H. T. Hattori, Strong coupling of exciton and high-Q mode in all-perovskite metasurfaces, *Adv. Opt. Mater.* **10**, 2101120 (2021).
- [43] C. Tian, L. Chen, Y. Zhang, L. Zhu, W. Hu, Y. Pan, Z. Wang, F. Zhang, L. Zhang, H. Dong, and W. Zhou, Relaxation oscillations of an exciton–polariton condensate driven by parametric scattering, *Nano Lett.* **22**, 3026 (2022).
- [44] C. Tian, B. Zhou, C. Xu, Y. Zhang, X. Zheng, J. Zhang, L. Zhang, H. Dong, and W. Zhou, Polariton–polariton interactions revealed in a one-dimensional whispering gallery microcavity, *Nano Lett.* **20**, 1552 (2020).
- [45] A. I. Kuznetsov, A. E. Miroshnichenko, M. L. Brongersma, Y. S. Kivshar, and B. Luk'yanchuk, Optically resonant dielectric nanostructures, *Science* **354**, aag2472 (2016).
- [46] Y. Fan, P. Tonkaev, Y. Wang, Q. Song, J. Han, S. V. Makarov, Y. Kivshar, and S. Xiao, Enhanced multiphoton processes in perovskite metasurfaces, *Nano Lett.* **21**, 7191 (2021).
- [47] See Supplemental Material at <http://link.aps.org/supplemental/10.1103/PhysRevApplied.18.014079> for additional information, which includes Refs. [48,49].
- [48] W. Zhou, M. Dridi, J. Y. Suh, C. H. Kim, D. T. Co, M. R. Wasielewski, G. C. Schatz, and T. W. Odom, Lasing action in strongly coupled plasmonic nanocavity arrays, *Nat. Nanotechnol.* **8**, 506 (2013).
- [49] S.-H. Chang and A. Taflove, Finite-difference time-domain model of lasing action in a four-level two-electron atomic system, *Opt. Express* **12**, 3827 (2004).
- [50] D. Zheng, S. Zhang, Q. Deng, M. Kang, P. Nordlander, and H. Xu, manipulating coherent plasmon–exciton interaction in a single silver nanorod on monolayer WSe₂, *Nano Lett.* **17**, 3809 (2017).
- [51] A. E. Miroshnichenko, A. B. Evlyukhin, Y. F. Yu, R. M. Bakker, A. Chipouline, A. I. Kuznetsov, B. Luk'yanchuk, B. N. Chichkov, and Y. S. Kivshar, Nonradiating anapole modes in dielectric nanoparticles, *Nat. Commun.* **6**, 8069 (2015).
- [52] K. As'ham, I. A. M. Alani, L. Xu, A. E. Miroshnichenko, and H. T. Hattori, in *2019 IEEE Photonics Conference (IPC)* (2019), pp. 1–2.
- [53] L. Xu, M. Rahmani, K. Zangeneh Kamali, A. Lamprianidis, L. Ghirardini, J. Sautter, R. Camacho-Morales, H. Chen, M. Parry, I. Staude, G. Zhang, D. Neshev, and A. E. Miroshnichenko, Boosting third-harmonic generation by a mirror-enhanced anapole resonator, *Light Sci. Appl.* **7**, 44 (2018).
- [54] A. Tripathi, H.-R. Kim, P. Tonkaev, S.-J. Lee, S. V. Makarov, S. S. Kruk, M. V. Rybin, H.-G. Park, and Y. Kivshar, Lasing action from anapole metasurfaces, *Nano Lett.* **21**, 6563 (2021).
- [55] S. Hu, Y. Ren, Y. Wang, J. Li, J. Qu, L. Liu, H. Ma, and Y. Tang, Surface plasmon resonance enhancement of photoluminescence intensity and bioimaging application of gold nanorod@CdSe/ZnS quantum dots, *Beilstein J. Nanotechnol.* **10**, 22 (2019).
- [56] A. Reserbat-Plantey, I. Epstein, I. Torre, A. T. Costa, P. A. D. Gonçalves, N. A. Mortensen, M. Polini, J. C. W. Song, N. M. R. Peres, and F. H. L. Koppens, Quantum nanophotonics in two-dimensional materials, *ACS Photonics* **8**, 85 (2021).